ACS APPLIED MATERIALS & INTERFACES

Research Article

www.acsami.org

Surface Chemistry of Perovskite-Type Electrodes During High Temperature CO_2 Electrolysis Investigated by *Operando* Photoelectron Spectroscopy

Alexander K. Opitz,*[,†] Andreas Nenning,[†,⊥] Christoph Rameshan,[‡] Markus Kubicek,[†] Thomas Götsch,[§] Raoul Blume,[∥] Michael Hävecker,[∥] Axel Knop-Gericke,[∥] Günther Rupprechter,[‡] Bernhard Klötzer,[§] and Jürgen Fleig[†]

[†]Institute of Chemical Technologies and Analytics, Vienna University of Technology, Getreidemarkt 9/164-EC, 1060 Vienna, Austria

[‡]Institute of Materials Chemistry, Vienna University of Technology, Getreidemarkt 9/165-PC, 1060 Vienna, Austria

[§]Institute of Physical Chemistry, University of Innsbruck, Innrain 80-82, 6020 Innsbruck, Austria

[∥]Department of Inorganic Chemistry, Fritz Haber Institute of the Max Planck Society, Faradayweg 4-6, 14195 Berlin, Germany

Supporting Information

ABSTRACT: Any substantial move of energy sources from fossil fuels to renewable resources requires large scale storage of excess energy, for example, via power to fuel processes. In this respect electrochemical reduction of CO_2 may become very important, since it offers a method of sustainable CO production, which is a crucial prerequisite for synthesis of sustainable fuels. Carbon dioxide reduction in solid oxide electrolysis cells (SOECs) is particularly promising owing to the high operating temperature, which leads to both improved thermodynamics and fast kinetics. Additionally, compared to purely chemical CO formation on oxide catalysts, SOECs have the outstanding advantage that the catalytically active oxygen vacancies are continuously formed at the counter electrode, and move to the working electrode where they reactivate the oxide surface without the need of a preceding chemical (e.g., by H_2) or thermal reduction step. In the present work, the surface chemistry of (La,Sr)$FeO_{3-\delta}$ and (La,Sr)$CrO_{3-\delta}$ based perovskite-type electrodes was studied during electrochemical CO_2 reduction by means of near-ambient pressure X-ray photoelectron spectroscopy (NAP-XPS) at SOEC operating temperatures. These measurements revealed the formation of a carbonate intermediate, which develops on the oxide surface only upon cathodic polarization (i.e., under sufficiently reducing conditions). The amount of this adsorbate increases with increasing oxygen vacancy concentration of the electrode material, thus suggesting vacant oxygen lattice sites as the predominant adsorption sites for carbon dioxide. The correlation of carbonate coverage and cathodic polarization indicates that an electron transfer is required to form the carbonate and thus to activate CO_2 on the oxide surface. The results also suggest that acceptor doped oxides with high electron concentration and high oxygen vacancy concentration may be particularly suited for CO_2 reduction. In contrast to water splitting, the CO_2 electrolysis reaction was not significantly affected by metallic particles, which were exsolved from the perovskite electrodes upon cathodic polarization. Carbon formation on the electrode surface was only observed under very strong cathodic conditions, and the carbon could be easily removed by retracting the applied voltage without damaging the electrode, which is particularly promising from an application point of view.

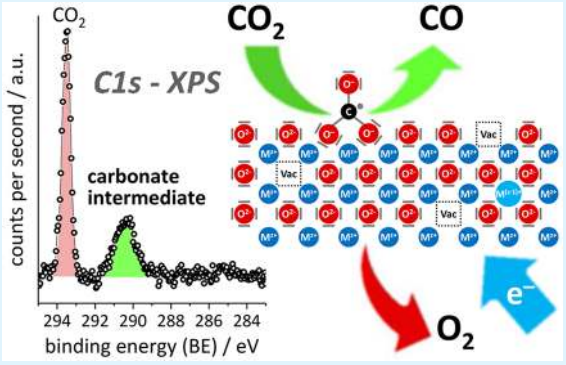

KEYWORDS: *solid oxide electrolysis cell, SOEC, mixed ionic electronic conductor, defect chemistry, CO_2 splitting, electron transfer, NAP-XPS, metal exsolution*

1. INTRODUCTION

In view of environmental problems such as global warming, it is one of the main scientific and technological challenges to improve possibilities for reducing emission of CO_2 while concurrently meeting the continuously rising energy demand of the population.[1,2] As a consequence, sustainable energy sources such as solar, wind, or hydroelectric power experience a strong upsurge. However, most of the renewable energy sources suffer from nonhomogeneous availability in both temporal and geographical senses. For a global change toward a carbon-neutral energy supply, the storage and distribution of sustainably produced energy is thus inevitable.

Electrolysis is a highly promising technology for fulfilling this need for energy storage, since it allows the transformation of

Received: July 20, 2017
Accepted: September 21, 2017
Published: September 21, 2017

DOI: 10.1021/acsami.7b10673
ACS Appl. Mater. Interfaces 2017, 9, 35847−35860

energy from a volatile source into a persistent form. Though electrolysis is currently often highlighted as a novel and innovative method for energy storage, its most popular example, the electrochemical splitting of water into hydrogen and oxygen, is already known since more than 200 years.[3] One of the main limiting factors for a widespread use of hydrogen as an energy carrier is its nontrivial storage[4] and the associated need to establish a new distribution infrastructure, which makes the change toward a hydrogen-powered society economically challenging. From a storage and distribution point of view, hydrocarbons offer a couple of advantages over hydrogen such as high volumetric energy density, safe and easy storability, and compatibility with existing fuel infrastructure.[4,5] One way out of this dilemma is hydrocarbon formation from H_2O and CO_2, which uses electrochemically produced hydrogen together with carbon dioxide via a methanation reaction ($CO_2 + 4H_2 \rightarrow CH_4 + 2H_2O$). This is commonly referred to as a power-to-gas (P2G) process. Another technologically relevant process for the synthesis of hydrocarbons is the Fischer−Tropsch process (e.g., $(2n + 1)H_2 + nCO \rightarrow C_nH_{2n+2} + nH_2O$), which, in contrast to the direct hydration of CO_2, is already industrially well-established. In current industrial large scale reactors, however, P2G methanation as well as Fischer−Tropsch and similar processes utilize locally available mixtures of CO_2, CO, and H_2, whereby the stoichiometric CO/H_2 ratio for the respective product needs to be established individually via a preceding reverse water−gas shift step (rWGSR: $CO_2 + H_2 \rightarrow CO + H_2O$).[6]

In contrast to this chemically driven CO_2 reduction, an electrochemically performed CO_2 splitting offers a couple of advantages: (i) No additional reduction agent such as H_2 is needed, which offers the possibility of higher efficiencies. (ii) Owing to the absence of both reducing agent (H_2) and byproduct (H_2O), no blocking of active sites by these species can occur, and the entire catalyst surface is available for CO_2 reduction. (iii) Contamination of the produced CO by the second product (H_2O in case of chemical reduction, O_2 in the electrochemical case) can easily be prevented via separating the gas compartments of working and counter electrodes. Electrolysis of CO_2 and H_2O thus offers a very attractive opportunity for avoiding the additional rWGSR step, allowing control of the final H_2/CO ratio (slightly above 2:1 for Fischer−Tropsch and methanol synthesis, 3:1 for synthetic methane) and, at the same time, utilizing excess renewable electricity. Consequently, electrolysis of CO_2 and H_2O, performed either separately or together as coelectrolysis, is highly attractive for running both power-to-gas and power-to-liquid processes using renewable resources with high efficiency. With sustainably produced CO and H_2 (commonly referred to as syngas) these processes thus offer the possibility of storing excess renewable energy in a form that is compatible with the existing fuel infrastructure. A further, though somewhat exotic, application of CO_2 electrolysis is the production of storable fuel as well as oxygen during space missions such as a long-term human exploration of planet Mars.[7,8]

Among the available types of CO_2 electrolyzers, the solid oxide electrolysis cell (SOEC) is the most promising one.[9] Owing to entropy reasons, its high operation temperature in the range of about 800 °C leads to a significant reduction of the cell voltage and thus to an increased efficiency.[5,10] From a kinetic point of view, carbon dioxide splitting in solution based electrolyzers is challenging owing to the very stable bonds in the CO_2 molecule[11] and the limited CO_2 solubility in aqueous electrolytes.[12] Moreover, CO_2 electrolysis cannot be done in proton exchange membrane (PEM) cells, since especially the product CO poisons the fuel electrode catalyst by very strong adsorption.[13] Also, in this respect, the high operation temperature of SOECs and the use of gas phases as reactants are highly advantageous. Typical electrode (SOEC cathode) materials for CO_2 reduction are Pt/YSZ,[7,14] Ni/YSZ,[10,15−18] and ceria based mixed conductors,[19−22] and perovskites such as $(La,Sr)(Cr,Mn)O_{3\delta}$[22−24] or donor doped $SrTiO_3$.[25] Most of the existing studies on high temperature CO_2 electrolysis were performed on porous electrodes in symmetrical cells or entire SOECs, aiming at an increase of the maximum current density.[7,10,14−25] In order to develop and improve efficient SOEC cathodes, a more detailed fundamental understanding of the kinetic processes and the mechanisms behind cathodic CO_2 reduction or CO_2 and H_2O co-reduction is required. However, studies on model systems with the goal of obtaining a detailed mechanistic understanding of the involved elementary processes are rare.[26−28] For gaining such an in-depth understanding of the surface chemistry of operating electrodes, the combination of electrochemical techniques and *operando* X-ray photoelectron spectroscopy (XPS) is a very powerful tool and thus has attracted much attention in recent years.[26,27,29−36] However, for CO_2 electrolysis again only very few studies exist. Those deal with model-type ceria based electrodes[26,27] while comparable mechanistic investigations on perovskite-type SOEC cathodes have, to the best of our knowledge, not been published so far.

Perovskite-type electrode materials could be a very attractive alternative to ceria based electrodes for CO_2 reduction since they offer a much larger compositional diversity and thus many options for optimizing the electrode stability, ionic and electronic conductivity, electrochemical properties, and catalytic activity.[37−41] In particular, the latter can be further affected by introduction of reducible transition metals, which may exsolve under reducing conditions, forming metallic particles on the perovskite surface.[38,41−47] In a recent study we could show by simultaneously performing electrochemical polarization experiments and near-ambient pressure XPS (NAP-XPS) measurements that the exsolution of metallic iron particles from $(La,Sr)FeO_{3\delta}$ electrodes strongly improves their water splitting kinetics.[36] It is an open question whether surface decoration of perovskite electrodes by exsolved metallic particles also improves CO_2 electrolysis.

In the present study we investigated the surface chemistry of perovskite-type oxides during carbon dioxide electrolysis by means of *operando* NAP-XPS measurements on $La_{0.6}Sr_{0.4}FeO_{3\delta}$ and $(La,Sr)(Cr,Ni)O_{3\delta}$ thin film model electrodes with different cation composition. The CO_2 reduction behavior of lanthanum ferrite based electrodes can be compared with their H_2O reduction properties reported recently.[36,48] The chromite based oxides were chosen since they offer the possibility of a reduction stable backbone[49−52] and exsolve Ni without the risk of decomposition as in the case of $La_{0.6}Sr_{0.4}FeO_{3\delta}$.[53] NAP-XPS revealed the voltage dependent evolution of different carbon species on the surface of the electrodes. Under cathodic polarization a carbon species at relatively high XPS binding energies (ca. 290 eV) can be observed, and its evolution is discussed in light of a possible reaction mechanism: A bidendate $(CO_3)^{\bullet 3-}$ adsorbate is suggested as the decisive intermediate of CO_2 activation. The formation of this surface species requires oxygen vacancies as well as electrons in the acceptor doped oxide electrode. Hence, perovskite-type oxides

DOI: 10.1021/acsami.7b10673
ACS Appl. Mater. Interfaces 2017, 9, 35847−35860

with high vacancy and high electron concentration might be particularly attractive for CO_2 electrolysis. As a second reduction process, the development of graphitic carbon was investigated, and it is shown that any carbon deposits can be removed by retracting the cathodic polarization, thus allowing for a complete recovery of the electrode performance. These insights into the relationships of surface chemistry and electrochemical performance not only provide a large step toward an in-depth understanding of CO_2 electro-reduction on perovskite-type oxides, but also provide a valuable basis for the future optimization of porous SOEC cathodes for CO_2 electrolysis, since the surface process on mixed conducting oxides is usually responsible for the largest contribution to the polarization resistance of "real" porous electrodes.

2. EXPERIMENTAL METHODS

2.1. Preparation of Materials. Three different compositions of chromite based perovskites were examined, see Table 1. Those were

Table 1. Composition of Investigated Perovskite-Type Working Electrodes and the Abbreviations Used

composition of perovskite electrode	abbreviation used throughout the text
$La_{0.6}Sr_{0.4}FeO_{3\delta}$	LSF
$La_{0.8}Sr_{0.2}Cr_{0.9}Ni_{0.1}O_{3\delta}$	LSCrNi8291
$La_{0.7}Sr_{0.2}Cr_{0.9}Ni_{0.1}O_{3\delta}$	LSCrNi7291
$La_{0.8}Sr_{0.2}CrO_{3\delta}$	LSCr

prepared as follows via a modified Pecchini method:[54] Appropriate amounts of $SrCO_3$ (99.995% trace metals basis, Aldrich) and La_2O_3 (99.99% trace metals basis, Aldrich) were dissolved in HNO_3 (redistilled, 99.999% trace metals basis, Aldrich); $Cr(NO_3)_3{\cdot}9(H_2O)$ (99.99% trace metals basis, Alfa Aesar) and, in case of Ni containing perovskites, $Ni(NO_3){\cdot}6(H_2O)$ (99.995% trace metals basis, Aldrich) were dissolved in double distilled water. The cation solutions were merged, citric acid (99.9998% trace metals basis, Aldrich) was added as a complexing agent in a molar ratio of 1.2 with respect to the total amount of cations, and the obtained solution was heated in a quartz beaker. After evaporation of large parts of the solvent a darkish foam was formed, which spontaneously decomposed upon further heating. The black residue was calcined at 750 °C in a box furnace, milled in a stainless steel mortar, isostatically pressed (ca. 4 kbar), and finally sintered at 1400 °C for 2 h in air to obtain targets for pulsed laser deposition (PLD). $La_{0.6}Sr_{0.4}FeO_{3\delta}$ (LSF) targets were prepared from commercial powder (purchased from Aldrich) by isostatic pressing (ca. 4 kbar) and sintering at 1250 °C in air.

2.2. Cell Preparation. The electrochemical cell was prepared by depositing electrodes on (100)-oriented 9.5 mol % yttria-stabilized zirconia (YSZ) single crystals (Crystec, Germany), which served as the electrolyte. For preparation of counter electrodes (CE), 20 mol % gadolinia doped ceria (GDC; Treibacher) paste, LSF paste, and Pt paste (Gwent Electronics) were consecutively brushed onto the bottom side of YSZ single crystals. GDC and LSF pastes were prepared from the respective powders, ethylcellulose, and terpineol by mixing them in a mortar. GDC was used to avoid reaction between LSF and YSZ and was sintered at 1300 °C. Subsequently, LSF and Pt paste were deposited and annealed for 2 h at 1050 °C in air. In these porous electrodes, LSF is the electrochemically active material and Pt acts as an electronic current collector. The GDC is a buffer layer to avoid formation of insulating zirconate phases at the LSF/YSZ interface during sintering at 1050 °C.

Thin film working electrodes (WE) of 200−250 nm thickness were grown at 650 °C on the polished top side of the YSZ electrolyte by pulsed laser deposition (PLD). To ensure a laterally homogeneous electron distribution and thus a well-defined electrochemical polarization of the thin film electrodes, a buried Pt current collector grid was fabricated prior to the PLD process by magnetron sputtering, photolithography, and Ar ion beam etching; more details on the working electrode preparation are given elsewhere.[36,48,55,56] Application of a GDC buffer layer between WE and YSZ was omitted since no zirconate formation is expected at temperatures of 800 °C and below. A sketch of the mounted sample's cross section and an electron microscopy image of a thin film working electrode with buried current collecting grid are depicted in Figure 1a,b, respectively.

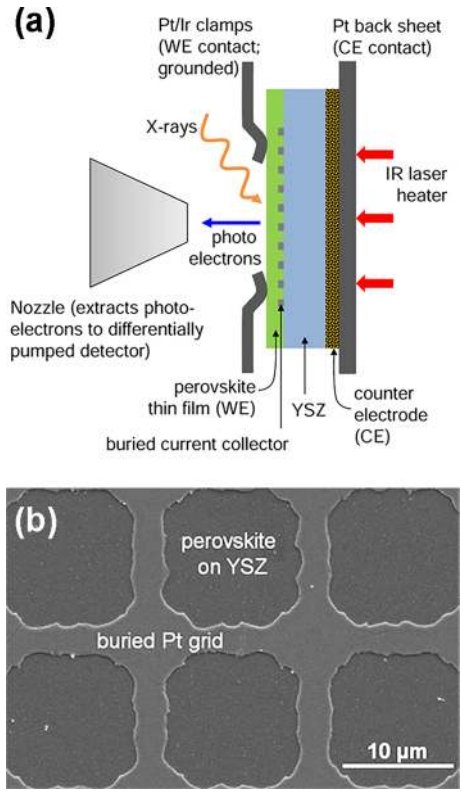

Figure 1. (a) Sketch (cross section) of an electrolysis cell mounted for NAP-XPS measurements. (b) SEM (top view) of a PLD-deposited LSF working electrode with embedded Pt thin film grid for current collection.

2.3. *Operando* NAP-XPS Experiments. NAP-XPS measurements were performed at beamline ISISS of synchrotron facility BESSY II in Berlin. The main part of the setup is a "high pressure cell" (up to 7 mbar), which is attached to a differentially pumped hemispherical analyzer (modified SPECS Phoibos 150); for details regarding the XPS equipment the reader is referred to ref 57. Photoelectron spectra were recorded with different photon energies (410 eV for C 1s, 490 eV for Ni 3s, 650 eV for O 1s, 845 eV for Fe 2p); pass energy was 20 eV. These correspond to kinetic photoelectron energies between 110 and 130 eV, which lead to an approximate information depth (inelastic mean free path) of ca. 0.5 nm. This is of the order of the rhombohedral lattice parameter of LSF,[53] thus allowing very surface sensitive measurements.

For mechanical fixation and electrical contact the electrochemical cell was mounted onto the Pt back plate of the sample holder by means of Pt/Ir clamps. The Pt/Ir clamps served both as mechanical fixations and electric contact of the working electrode. The Pt back plate contacted the counter electrode. A sketch of such a cell mounted for spectroscopy is shown in Figure 1a. Heating of the cell was done by illuminating the CE-sided Pt sheet with an IR laser. Temperature was controlled by adjusting the power of the infrared laser heating the back plate of the sample holder. Temperature measurement was done by a pyrometer as well as by the ionic conductivity of the YSZ electrolyte obtained from impedance measurements; details regarding the latter procedure are given in refs 58 and 59. Temperature values resulting from both methods were in reasonable agreement of ±15 °C. For

DOI: 10.1021/acsami.7b10673
ACS Appl. Mater. Interfaces 2017, 9, 35847−35860

electrochemical polarization experiments as well as impedance spectroscopy, a Novocontrol Alpha Analyzer equipped with a POT/GAL interface was used. For these measurements the WE was grounded, and the voltage was applied to the counter electrode. The overpotential η at the WE was obtained by subtracting the ohmic drop in the electrolyte (and the contact resistances and wires) from the applied voltage U_{set} by

$$\eta = -(U_{set} - R_{ohm} \times I_{DC}) \quad (1)$$

In eq 1 R_{ohm} denotes the ohmic resistance (obtained from the high frequency intercept in impedance spectra, see Figures S1 and S2 in the Supporting Information), and I_{DC} is the steady state DC (direct current) current flowing during polarization experiments. The potential drop at the counter electrode is small compared to the thin film working electrode by the following considerations: (i) The surface area of the porous CE is large compared to the surface area of the thin film electrode; thus, the polarization resistance of the porous CE can be regarded to be rather small compared to the WE. (ii) The CE acts as an oxygen evolution electrode during CO_2 splitting at the WE (as can be seen from MS data below), and its polarization resistance for this reaction was already shown to be negligible.[48] Consequently, the CE also acts as a reversible reference electrode, thus allowing two-point measurements. For all experiments, the background pressure in the chamber was 0.25 mbar CO_2. The gas composition in the chamber was measured by a quadrupole mass spectrometer (Pfeiffer Prisma). Please note that all the experiments were performed in a single chamber setup, i.e., without separation of anodic and cathodic gas compartments. Thus, both gaseous products of CO_2 electrolysis (O_2 and CO) can be found in the chamber (further details see Section 3.1).

3. RESULTS AND DISCUSSION

3.1. Electrochemical and MS Results. In a first step, we demonstrate that electrochemical CO_2 reduction indeed takes place upon cathodic polarization. A plot of the electrochemical DC current I_{DC} versus the overpotential η applied to the thin film working electrode is depicted in Figure 2. This diagram shows a comparison of all investigated perovskite-type materials at 720 °C in 0.25 mbar CO_2. For a mixed conducting electrode with surface limited kinetics the overpotential η determines the deviation of the oxygen chemical potential in the electrode from its equilibrium value ($\Delta\mu_O$), i.e., the difference between the chemical potential of oxygen in the electrode ($\mu_{O,el}$) from the value in the gas phase ($\mu_{O,gas}$). This is the thermodynamic driving force of the reaction:[48]

$$\Delta\mu_O = \mu_{O,el} - \mu_{O,gas} = 2F\eta \quad (2)$$

The DC current I_{DC} is a direct measure of the reaction rate r since in the case of a purely ionic current through the electrolyte both are connected by Faraday's law

$$I_{DC} = z \times F \times r \quad (3)$$

with z and F denoting the number of transferred electrons and Faraday's constant, respectively. In our case the reaction rate is the rate of CO_2 reduction at the SOEC cathode (i.e., working electrode)

$$CO_2 + 2e^- \rightarrow CO + O^{2-} \quad (4)$$

and owing to charge neutrality also the rate of oxygen evolution at the anode (i.e., counter electrode)

$$O^{2-} \rightarrow 1/2O_2 + 2e^- \quad (5)$$

The total CO_2 electrolysis reaction, which is the sum of both partial reactions, is thus

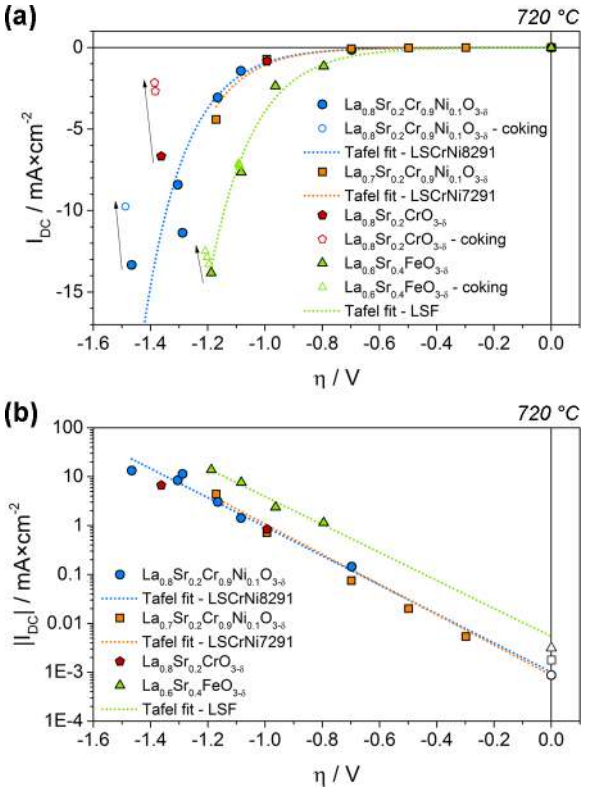

Figure 2. Current−overpotential characteristics of the four different WE materials measured at 720 °C in 0.25 mbar CO_2. (a) Linear plot. The filled symbols are regular data points. The open symbols indicate measurements influenced by deposition of graphitic carbon (owing to large cathodic overpotentials). The corresponding degradation of the current is indicated by the arrows. The lines indicate the curves obtained from fitting the data in the logarithmic diagram below. (b) Tafel plot, i.e., logarithmic $I-V$ characteristics, of the data in part a. Data points influenced by carbon deposition related degradation are not shown. The lines were obtained by fitting the data points to the Tafel equation (see eq 7b). The open points at η = 0 V were not considered in these fits.

$$CO_2 \rightarrow CO + 1/2O_2 \quad (6)$$

From Figure 2a, a higher activity of LSF for CO_2 splitting can be concluded, since it shows similar electrolysis currents as the chromite based materials already at ca. 200 mV lower polarization; i.e., a lower thermodynamic driving force is needed for the same reaction rate.

The shape of the measured curve indicates an exponential relation between I_{DC} and η. A logarithmic plot of the current versus the overpotential, which is commonly referred to as the Tafel plot, thus yields a linear correlation (see Figure 2b). This can be analyzed in terms of

$$I_{DC} = -I_0 e^{-\alpha F/RT\eta} \quad (7a)$$

or

$$\log|I_{DC}| = \log|I_0| - \alpha\frac{F}{RT}\log(e)\eta \quad (7b)$$

with R and T denoting gas constant and absolute temperature, respectively. The fit parameter I_0, which can be extracted from the axis intercept of the linear curve in Figure 2b, is the exchange current density under equilibrium conditions. It is connected to the equilibrium exchange rate of the CO_2 reduction reaction (eq 3) by Faraday's law (eq 2). Such an

DOI: 10.1021/acsami.7b10673
ACS Appl. Mater. Interfaces 2017, 9, 35847−35860

exponential relation between current and overpotential is frequently found in electrochemistry, and in aqueous electrochemistry this often indicates a rate-limiting charge transfer.[60] However, a simple interpretation of such a relation may fail for electrochemical reactions at gas/solid interfaces.[61] Not only does the overpotential η differ from the relevant change of the surface potential step, but also the variation of defect concentrations by applying a voltage ($\eta = \Delta\mu_O/2F$) may be highly important.[62] Hence, also the meaning of the parameter α in eq 7 is not straightforward. Fit parameters are summarized in Table 2.

Table 2. Resulting Fit Parameters of Tafel Fits in Figure 2b (720 °C data) Using Equation 7b

material	α	I_0/mA cm^{-2}
LSCrNi8291	0.590 ± 0.025	(10.1 ± 1.4) × 10^{-4}
LSCrNi7291	0.613 ± 0.045	(8.7 ± 1.6) × 10^{-4}
LSF	0.567 ± 0.066	(54 ± 18) × 10^{-4}

As already mentioned above, these results reveal LSF as the more active material: Its exchange current density is almost 1 order of magnitude higher than those of the chromite based components. The difference in α of all materials, however, is statistically insignificant. This is a clear indication that the rate-determining step is of the same nature on all investigated perovskite-type WEs. The difference in I_0 between LSF and LSCrNi may be caused by a different height of the activation barrier and/or by a different concentration of a species involved in the rate-determining reaction step. Correlation of these results with NAP-XPS data suggests that different defect concentrations (electrons and oxygen vacancies) are the more likely reason (see discussion below).

Moreover, the results in Figure 2 strongly suggest that the exsolution of metallic particles does not play a significant role for the CO_2 electrolysis performance, since the Ni free chromite electrode (red pentagons in Figure 2) shows almost the same electrochemical behavior as the Ni containing ones (blue circles). Exsolution of metallic Ni from LSCrNi was verified by NAP-XPS (see Section 3.2 below) as well as by SEM images (Figure S4 in the Supporting Information). The maximum catalytic effect of the Ni exsolutions (if there is any) is thus smaller than the experimental scatter between nominally identical samples. This is very little compared to that of H_2O electrolysis, which is accelerated by more than an order of magnitude once metallic exsolutions are formed.[36,47] Further details on the role of exsolved metal particles for CO_2 electrolysis will be discussed in the following sections.

For LSCrNi7291 and LSF, $I-V$ curve measurements were also performed at 600 and 400 °C, respectively. The resulting Tafel plots are shown in Supporting Information Figure S3. The corresponding fit results are summarized in Table S1. Thus, a first estimate of activation energies of I_0 can be made for LSCrNi7219 and LSF and leads to 1.7 and 1.3 eV, respectively. This difference in activation energy can originate from a different energy barrier height or a different formation enthalpy of a species in the rate-determining reaction step or from a combination of both.

Since the above-mentioned interpretations are only valid for a Faradaic relation between I_{DC} and reaction rate, the gas composition in the reaction chamber was analyzed by mass spectrometry (MS). Owing to the large background of CO_2 and its fragmentation into CO the accurate measurement of the reaction product CO was rather challenging.[63] However, since the experiments were performed in a single chamber setup, both products of the electrolysis reaction CO and O_2 (which are connected by eq 6) are observable. Thus, not only the CO but also the O_2 signal can be used to check for a linear relationship with the DC current. Plots of the normalized O_2 signal versus the DC current are depicted in Figure 3a,b for

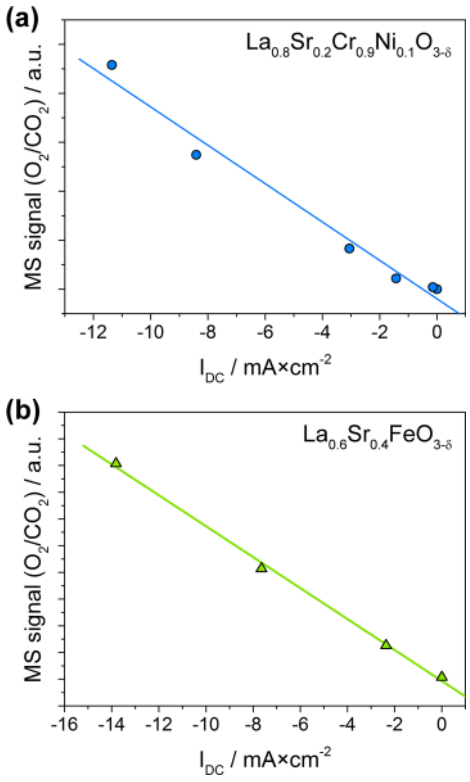

Figure 3. MS signal of oxygen normalized to the CO_2 background plotted as a function of the measured DC current at 720 °C in 0.25 mbar CO_2 for (a) LSCrNi8291 working electrode and (b) LSF working electrode. The lines indicate a linear fit in each case.

LSCrNi8291 and LSF, respectively. In either case a linear correlation between the amount of produced oxygen and the electrochemical current is found. This is a strong indication of a Faradaic electrolysis of CO_2 despite rather strong cathodic polarization. Contributions of an electronic current in YSZ, which may become relevant for strongly reducing conditions,[64] can thus be neglected.

Furthermore, it should be noted that for very high polarization a time dependent decrease of the electrolysis current can be observed, which is indicated by the open symbols as well as by the arrows in Figure 2a. This degradation can be related to the deposition of graphitic carbon, which was observed by NAP-XPS measurements; see Section 3.6 for spectroscopic details. However, both the degradation and the presence of surface carbon were completely reversible upon retracting the applied electrochemical potential. At the experimental temperature of 720 °C the reaction of carbon with carbon dioxide via Boudouard's reaction ($C + CO_2 \rightleftarrows 2CO$) already yields significant amounts of CO[65] and is obviously sufficiently fast for regenerating all materials used in this study. This observation is particularly important from an application point of view, since it offers a rather simple method of resetting degradation caused by coking. Further details

DOI: 10.1021/acsami.7b10673
ACS Appl. Mater. Interfaces 2017, 9, 35847−35860

regarding coking and regeneration of the working electrodes and corresponding XPS data are discussed in Section 3.6.

3.2. NAP-XPS Results. At each applied electrochemical polarization (i.e., each point in Figure 2) NAP-XPS measurements were performed. Here, the main focus was laid on the measurement of C 1s and O 1s spectra. Typical C 1s spectra of all four perovskite-type working electrodes under polarization are depicted in Figure 4. Depending on the electrochemical

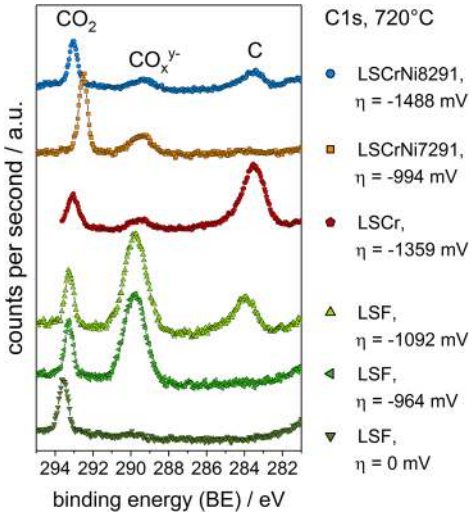

Figure 4. Comparison of C 1s spectra measured on the four different perovskite-type working electrodes at 720 °C in 0.25 mbar CO_2 under different cathodic polarizations. In this plot binding energies were corrected by the applied overpotential for the sake of easier comparability of different spectra assuming a shift of the electrode's Fermi level upon polarization by −1 eV/V.[31,48] (This correction anticipates a result, which is discussed later in the text.)

polarization, different features could be observed, corresponding to different carbon species. Qualitatively, however, the four different materials showed a very similar behavior.

Without additional polarization, only one sharp C 1s peak at 293−294 eV could be detected. Since this peak can be suppressed by applying a DC bias to the nozzle of the photoelectron collecting aperture (see Figure S5) and owing to its characteristic binding energy,[66] it can be identified as a CO_2 gas phase signal. Upon application of a cathodic overpotential to the WE, this gas phase signal is slightly shifted, and an additional broader peak appears at ca. 290 eV (indicated by CO_x^{y-} in Figure 4). This additional species is most probably decisive for CO_2 reduction; owing to its position in the spectrum it may be a carbonate or carboxylate[67] or a related oxygenated carbon species. Further investigation and discussion of its nature and kinetic implications is the subject of the following sections. The shift of the gas phase peak can be explained by a change of the vacuum level gradient within the gas phase upon electrochemical polarization of the working electrode.[29,68,69] At very high cathodic overpotential, a further carbon species appears on the electrode surface as can be observed by the evolution of another C 1s peak at ca. 284 eV (indicated by C in Figure 4). Owing to its position in the spectrum and its asymmetric shape, this species can be clearly identified as graphitic carbon.[66,70]

Interestingly, the appearance of the carbon species at ca. 290 eV also finds its counterpart in O 1s spectra, which is illustrated for a LSCrNi7291 electrode in Figure 5. It shows a comparison

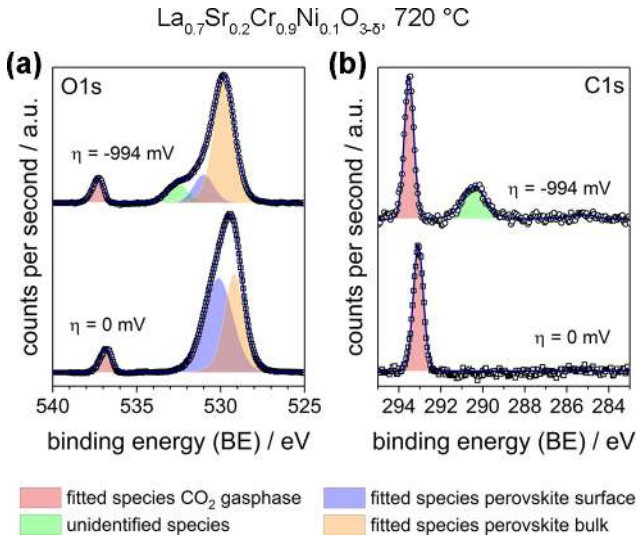

Figure 5. Comparison of O 1s spectra (a) as well as C 1s spectra (b) of cathodically polarized (○) and nonpolarized (□) LSCrNi7291 working electrode at 720 °C in 0.25 mbar CO_2. In the case of both types of spectra, an additional feature is visible upon polarization (top spectrum in each case). The components used for fitting are indicated as the filled peak areas, and the envelope of the fit is the solid blue line. (BE was not corrected to visualize peak shifts.)

of O 1s (Figure 5a) and C 1s (Figure 5b) spectra for the polarized (top) and nonpolarized (bottom) situation. The appearance of the carbon species peak at ca. 290 eV is clearly accompanied by the evolution of a shoulder at ca. 532 eV in the O 1s spectrum, and this further supports an interpretation of this species in terms of a carbon−oxygen compound. Moreover, in Figure 5 the fit results of individual components are indicated as colored peak areas below the curve. For fitting of O 1s spectra, up to four components were used: the CO_2 gas phase at ca. 537 eV and two components to fit the signal from the perovskite at ca. 530.5 and 529 eV, which are interpreted in literature studies as surface and bulk oxygen species, respectively.[32,71−73] Moreover, one additional species accounts for the shoulder appearing at ca. 532 eV in the case of polarized electrodes. Further details on the fitting procedure of O 1s and C 1s spectra are given in the Supporting Information.

Please note that owing to the absence of a Fermi edge for most of the samples no binding energy correction for all of the spectra in this study was performed. The meaning of this approach should be briefly explained: Since the WE electrode was grounded, electrostatic charging can safely be excluded as a source of the XPS peak shift. The observed shifts are thus either due to chemical shift (for example different species in C 1s and O 1s spectra) or due to work function changes caused by changes of electron concentration (i.e., shift of the Fermi level), which is a result of the electrochemical polarization.[31,48] For the sake of better comparability the spectra in Figure 4 are corrected for the latter effect. However, the fitting of data was performed on uncorrected data, since the Fermi level shift upon polarization itself is an interesting result, which is analyzed and discussed in detail below. To estimate the accuracy and the scatter of our nominally uncorrected binding energies, which arise, e.g., from monochromator mechanics at the beamline,[74] the carbon peak in C 1s spectra was used. In our case a mean value of 284.99 eV with a standard deviation of 0.18 eV results, which is in good agreement with literature values for disordered graphitic carbon.[70]

DOI: 10.1021/acsami.7b10673
ACS Appl. Mater. Interfaces 2017, 9, 35847−35860

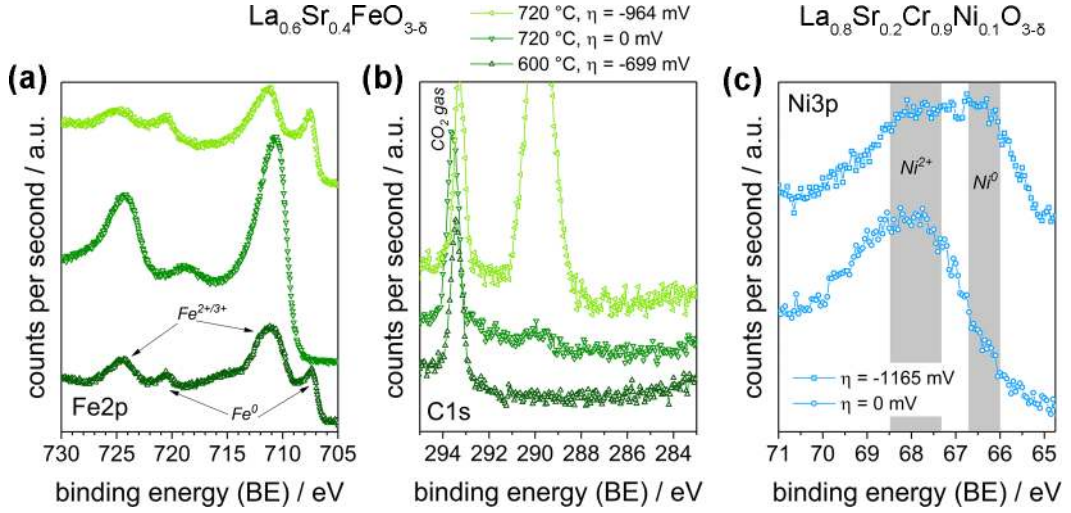

Figure 6. Comparison of Fe 2p (a) and C 1s (b) spectra measured on LSF electrodes at 600 °C in 0.25 mbar CO_2 at a cathodic polarization of −299 mV. In Fe 2p clearly the signature of both oxidic and metallic iron can be observed; in C 1s only the sharp peak of the CO_2 gas phase is present (BE in C 1s spectra were corrected by η for the sake of easier comparability). (c) Ni 3p spectra measured on LSCrNi8291 at 720 °C with and without cathodic polarization showing the exsolution of Ni at the electrode surface (BE corrected by η). The gray shaded areas indicate typical 3p binding energies for metallic nickel and Ni^{2+} in oxides.[75,76]

3.3. Identification of the Surface Species Appearing under Cathodic Polarization. To answer the question about the nature of the oxy-carbon adsorbate evolving under cathodic polarization, it is helpful to first discuss where, i.e., on which substrate, it is adsorbed. In principle, two different cases are possible:[11] adsorption on the perovskite-type oxide or on the exsolved metal particles. The latter case can be ruled out by two arguments: First, the appearance of the unidentified species does not correlate with the formation of a metallic species since, on LSF at 600 °C, η = −699 mV, already substantial amounts of metallic iron can be detected, whereas no C 1s signal at 290 eV can be observed in the C 1s spectrum. On the other hand, at 720 °C a small though observable signal at ca. 290 eV is visible in C 1s spectra already without polarization and thus without presence of metallic iron, cf. parts a and b of Figure 6. Second, the carbon species at ca. 290 eV also appears on LSCr electrodes, which do not contain any cations that may form metallic exsolutions, see Figure 4 (red pentagons). Consequently, the species can be assigned to the oxide.

This irrelevance of the exsolved metal particles for CO_2 electrolysis is also obvious from the electrochemical data in Figure 2. The presence of metallic nickel on the Ni doped chromite electrodes under cathodic conditions was confirmed by evolution of a lower energy species in Ni 3p spectra, see Figure 6c. (Please note that a measurement of Ni 2p was not possible owing to an overlap with La 3d lines.) This seems to contradict the assumption of an enhanced catalytic activity of exsolved Ni for CO_2 electrolysis as published in recent studies.[33,77] One reason may be the different oxide/metal combinations investigated in the present work and the above cited literature studies. At least on chromite electrodes in a H_2/H_2O atmosphere, exsolution of Ni particles caused a much smaller enhancement effect on the electrochemical performance than Ru exsolution.[78] However, for CO_2 splitting, to the best of our knowledge, such an effect was not reported so far. Thus, the most obvious difference between the present work and the literature studies on CO_2 electrolysis employing Ni exsolution electrodes appears to be the comparably ill-defined surface areas of the porous electrodes, which were used in refs 33 and 77. The dependence of the inner surface of porous electrodes on the sintering behavior of the starting powder, which may be affected by composition changes such as addition of exsolvable transition metals, makes normalization of measured currents to the correct electrode surface area rather challenging and prone to systematic errors. Indeed, the claimed effects on the electrode performance in refs 33 and 77 are only in the range of 10%, which may be explainable by differences in inner surface of porous electrodes. Moreover, XPS measurements in ref 33 were conducted *ex situ*, thus not allowing the detection of a metastable adsorbate, which only forms under operation conditions. This result again highlights the importance of using geometrically well-defined model electrodes in combination with *operando* spectroscopic characterization for a detailed investigation of the relevant electrode surface chemistry.

Further strong evidence that the unidentified species is indeed adsorbed on the oxide is its binding energy shift upon electrochemical polarization. In Figure 7a the difference between the C 1s binding energies of the adsorbate and graphitic carbon is plotted versus the applied overpotential. Graphitic carbon is assumed to form an additional phase on top of the electrode, and thus, its Fermi level cannot be affected by defect chemical changes in the electrode. A linear fit including data points from all materials yields a slope of almost exactly −1 eV/V. (Please note that the error of the slope can almost exclusively be explained by the standard deviation of our non-normalized binding energy values, which amounts to 0.18 eV, cf. Section 3.2). This clearly shows that the species is associated with the perovskite lattice, since it almost exactly follows the shift of the Fermi level, which is a consequence of the electrochemical polarization in our predominantly vacancy-compensated mixed conducting electrodes.[31,48] The slope of almost exactly −1 eV/V in Figure 7a is thus a strong argument for ruling out the possibility of the 290 eV peak in C 1s spectra to originate from a gaseous species. Even though gas phase signals also show polarization induced shifts,[68,69] the changes in binding energy are significantly smaller as can be seen in Figure S6 in the Supporting Information. Moreover, the rather broad peak shape of the CO_x^{y-} species provides further evidence of its

DOI: 10.1021/acsami.7b10673
ACS Appl. Mater. Interfaces 2017, 9, 35847−35860

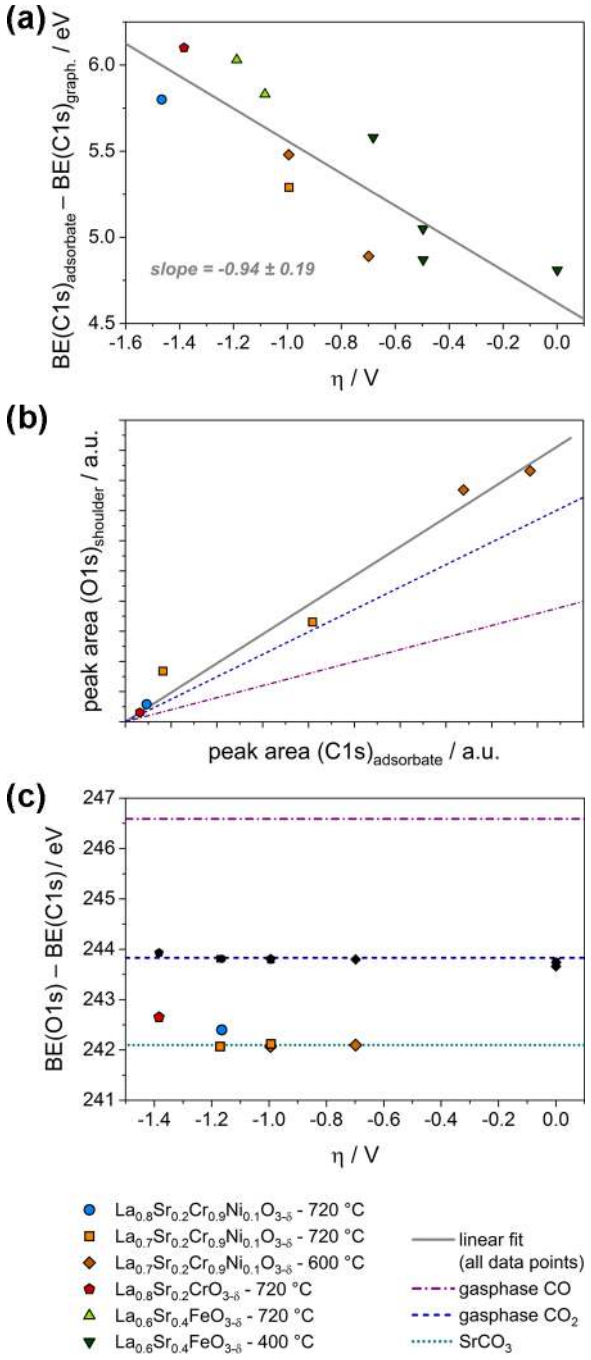

Figure 7. (a) Difference between the binding energy of the unidentified C 1s species at ca. 290 eV and graphitic carbon plotted versus the applied overpotential. The solid line is a linear fit considering all data points. (b) Plot of the XPS peak area of the shoulder in O1s spectra at 532−533 eV versus the peak area of the species in C 1s at ca. 290 eV. The solid gray line is a linear fit considering all data points. The dashed and the dash-dotted line indicate the corresponding peak area ration from CO_2 and CO gas phase measurements, respectively. (c) Difference in binding energy of the unidentified species in O 1s and C 1s spectra plotted versus the applied overpotential. The dashed and the dash-dotted line indicate the corresponding values from CO_2 and CO gas phase measurements, respectively. The black symbols indicate the values extracted from the CO_2 gas phase peak of "regular" NAP-XPS measurements (i.e., performed on perovskite electrodes). The dotted line indicates the corresponding BE difference between O 1s and C 1s reported for $SrCO_3$.[80,81]

adsorbate character, since gas phase peaks are usually sharper, such as the CO_2 peak in Figures 4−6.

Additional information for identifying the nature of the adsorbate appearing upon polarization comes from its oxygen to carbon ratio. In Figure 7b the peak area of the O 1s shoulder at ca. 532 eV BE is plotted versus the peak area of the C 1s peak at ca. 290 eV BE (cf. also Figure 5). With the assumption of a linear relationship, the obtained fit curve (solid gray line in Figure 7b) is significantly steeper than the expected slopes extrapolated from CO_2 and CO gas phase measurements shown by the dashed and dash−dotted lines, respectively. After correcting the C 1s/O 1s area ratio of the fit curve by the X-ray intensities at different photon energies as well as by the different probabilities of photoelectron emission of the two different elements,[79] an oxygen to carbon ratio of 2.84 ± 0.15 can be obtained. A very similar value (ca. 2.8) was obtained for intensity calibration by the gas phase peaks of CO_2, which have a molar ratio of 1:2. This result of a value rather close to 3 strongly suggests that both the 290 eV peak in C 1s spectra and the O 1s shoulder at ca. 532 eV can be attributed to a carbonate species. This interpretation of a carbonate adsorbate is further supported by the difference in binding energy of the corresponding O 1s and C 1s signals, which is shown in Figure 7c. Comparison with gas phase CO and CO_2 as well as bulk $SrCO_3$[80,81] clearly identifies its carbonate nature.

3.4. Polarization Dependence of the Surface Carbonate. In Figure 8 the evolution of the peak area of the carbonate XPS signal with overpotential η is depicted. Under moderate cathodic polarization the amount of carbonate quickly increases. The observations that the formation of the carbonate only occurs under cathodic polarization and that the surface coverage first increases upon increasing the polarization indicate an electron transfer to be necessary to form the surface carbonate. In other words the presence of electrons in the semiconductor-type oxide is crucial for the formation of the surface carbonate. This increase in electron concentration upon electrochemical polarization is also reflected by the observed −1 eV/V slope in Figure 7a, which is caused by an increase of the Fermi level of the perovskite under cathodic polarization.[31,48] It should also be emphasized that the formation and/or increase of the amount of surface carbonate cannot be explained by a change of the vacancy concentration, since under the applied conditions the acceptor dopant is already to a large

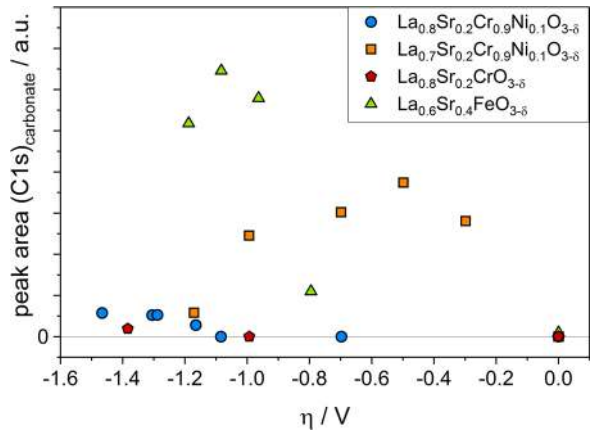

Figure 8. Peak area of the carbonate C 1s peak plotted as a function of the applied overpotential for four different electrode materials measured at 720 °C in 0.25 mbar CO_2.

DOI: 10.1021/acsami.7b10673
ACS Appl. Mater. Interfaces 2017, 9, 35847−35860

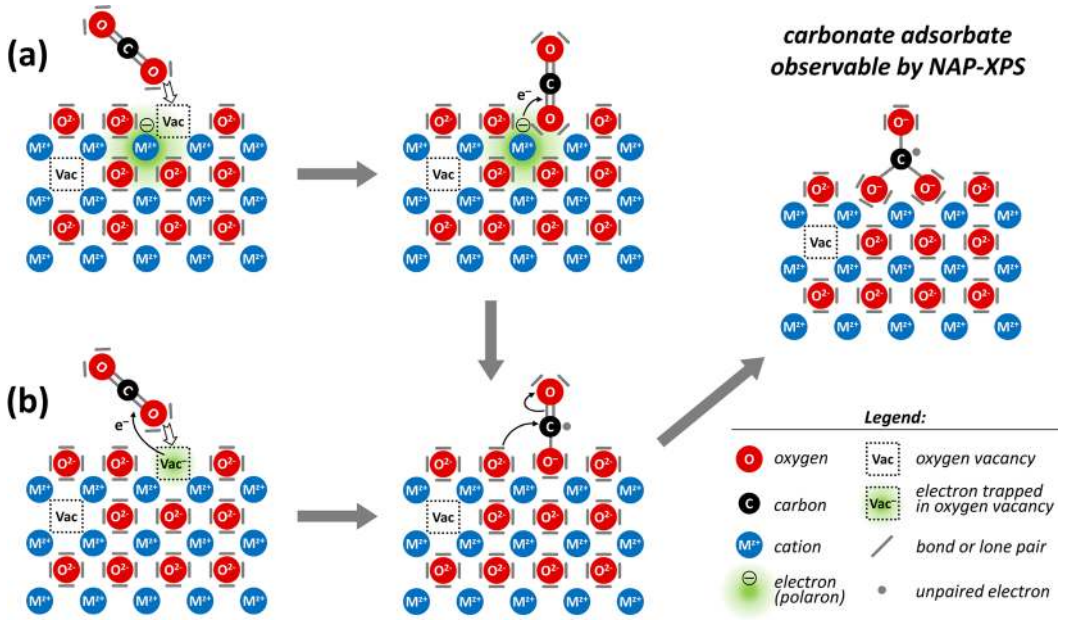

Figure 9. Sketch of the proposed mechanism of the formation of the carbonate adsorbate detected by NAP-XPS. For the sake of simplicity only a cut through a (100) lattice plane occupied by B and O, with the surface parallel to (110), is depicted, thus not showing the full perovskite structure. (a) CO_2 adsorbing into an oxygen vacancy, followed by an electron transfer from a polaron (or the conduction band). (b) CO_2 adsorption and first electron transfer occurring in one step by adsorption into a singly charged oxygen vacancy (i.e., a vacancy with a trapped electron). In either case a or b, a bidentate carbonate radical results, which is regarded as a reaction intermediate of CO_2 reduction to CO.

degree vacancy compensated (especially in case of LSF).[53] Consequently, a further reduction cannot significantly increase the oxygen vacancy concentration since vacancies are already majority charge carriers.

Upon further increasing the cathodic polarization the carbonate coverage reaches a plateau; see LSF (green triangles) and LSCrNi7291 (orange squares) in Figure 8. A maximum amount is found for LSF and LSCrNi7291, while in the case of LSCrNi8291 (blue circles) only the onset of the plateau is visible since carbon deposition started at very high cathodic voltages thus impeding further measurements of the carbonate species under higher polarization values. Interestingly, this plateau in carbonate surface coverage differs by almost 1 order of magnitude between the different perovskites, see Figure 8. This can be interpreted in terms of different number of available adsorption sites. From a defect chemical point of view the most obvious difference between the materials is their degree of acceptor doping (with LSF > LSCrNi7291 > LSCrNi8291 ≈ LSCr). Consequently, they exhibit significantly different concentrations of oxygen vacancies under reducing conditions. Assuming oxygen vacancies as the adsorption sites for CO_2 may thus partly explain the trend of different saturation limits in Figure 8. Moreover, the existence of a saturation limit also suggests a rate-limiting elementary step subsequent to carbonate formation.

For LSF and LSCrNi7291 the carbonate coverage is observed to decrease again under very high cathodic bias; see green triangles and orange squares in Figure 8, respectively. This behavior suggests the rate-limiting step subsequent to carbonate formation also depends on the electron concentration of the mixed conducting electrode material. A second electron transfer leading to electrochemical carbonate reduction would be a potential explanation for this polarization induced carbonate decomposition.

3.5. Discussion of the Mechanism of CO_2 Electrolysis on Perovskite-Type Electrodes. Before a mechanism is suggested, the most important observations should be briefly summarized:

- The formation of the carbonate correlates with an increasing electron concentration in the perovskite electrodes. Thus, an electron transfer is concluded to be necessary to form the carbonate. Since the carbonate only exists under sufficiently cathodic polarization but immediately vanishes upon retracting the bias, it is regarded as an intermediate of carbon dioxide reduction.
- The maximum coverage of the surface carbonate shows the same trend as the oxygen vacancy concentration in the investigated materials, which suggests oxygen vacancies as the adsorption sites of CO_2 forming the surface carbonate. Moreover, the saturation behavior suggests that an elementary step of the carbonate reduction to CO rather than the carbonate formation is rate-limiting.
- The carbonate coverage again decreases under very high electrochemical polarization, which is an indication that also the rate-limiting step of carbonate reduction to CO can be accelerated by cathodic polarization.

To consider both oxygen vacancies as well as electronic charge carriers in the formation of the carbonate, adsorption of CO_2 to an oxygen vacancy at the surface (denoted Vac), coupled with an electron transfer, is suggested as the first step of carbonate formation:

$$CO_2(gas) + Vac + e^- \rightarrow (CO_2)^{\bullet -}(ad) \quad (8)$$

The corresponding electron can either originate from a near surface polaron, e.g., a reduced Fe^{2+} or Cr^{2+} ion, or may already reside in the vacancy. In the first case the electron may be delocalized on the B−O sublattice of the perovskite owing to possible hybridization of the metal-d and oxygen-p states.[31,82]

DOI: 10.1021/acsami.7b10673
ACS Appl. Mater. Interfaces 2017, 9, 35847−35860

The latter case corresponds to an electron being trapped in the oxygen vacancy thus forming a singly charged vacancy ($Vac + e^- \rightarrow Vac^-$). This defect species is reported in oxygen deficient oxides under strongly reducing conditions and may even act as a color center.[64,83−85] Owing to the electronic structure of CO_2, the resulting species needs to be a radical (indicated by • in eq 8; please do not confuse this with the relative charge in Kröger−Vink notation for point defects). In a following step, the carbonate can be formed by bonding to another surface oxide ion forming a bidentate carbonate:

$$(CO_2)^{\bullet-}(ad) + O^{2-} \rightarrow (CO_3)^{\bullet 3-}(ad) \quad (9)$$

The interpretation of the carbonate as a bidentate is thus a direct consequence of the suggested CO_2 adsorption to a surface vacancy. A sketch of the reactions in eqs 8 and 9 is depicted in Figure 9. The weakening of the bonds associated with the radical nature of the carbonate may be responsible for the activation of the rather stable CO_2 molecule. The fact that no intermediate before $(CO_3)^{\bullet 3-}$ formation can be detected by NAP-XPS indicates a low surface coverage of the respective species. It even appears to be the general case for all investigated perovskites that only one reaction intermediate exhibits a measurable surface coverage.

It should further be emphasized that formation of the suggested bidentate is not equally realistic on every perovskite surface, since the distance of two oxygen lattice sites needs to be in a certain range to allow for bidentate adsorption. The C−O bond length in a regular CO_3^{2-} ion is 1.28 Å, and the O−O distance is ca. 2.22 Å.[86,87] Owing to the absence of a double bond in the proposed $(CO_3)^{\bullet 3-}$ adsorbate, the bond lengths and thus the O−O distance can be expected to be slightly longer. With a comparison of these numbers with the oxygen lattice site distances in our pseudocubic perovskites, an adsorption on a AO-terminated (100) facet with an oxygen−oxygen distance between 3.8 and 3.9 Å is hardly possible. On a BO-terminated (100) facet, however, the distance between two neighboring oxygen sites is smaller by a factor of $1/\sqrt{2}$ and thus in the range of 2.7 Å. Consequently, the adsorption of the suggested carbonate radical would be feasible on such a surface at least from a sterics point of view. AO-terminated (110) or oxygen-terminated (111) facets are other examples of perovskite surfaces capable of carbonate bidentate formation.

To the best of the authors' knowledge, such a carbonate species has not been reported so far for perovskite-type electrodes. However, similar results were described for Gd and Sm doped ceria thin film electrodes.[26,27] In both studies an adsorbed species on ceria was identified as a carbonate. Also there, the carbonate intensity increased with cathodic overpotential, and its coverage was saturated under strong cathodic polarization. Moreover, in ref 27, the carbonate species is also interpreted as a surface carbonate with an excess electron, which is further reduced to CO in a following rate-determining step. In contrast to our interpretation, the resulting carbonate is suggested to be adsorbed on the ceria surface as a monodentate. While not being stable as a bulk species, such a carbon dioxide or carbonate adsorbate with excess negative charge has already been discussed in surface science, and it was suggested to play a role in CO_2 activation.[11] The authors of ref 27 identified Ce^{3+} on the ceria surface as the crucial electron delivering point defect. These Ce^{3+} point defects are in fact electrons, which are localized on a Ce^{4+} ion, i.e., polarons.[88] Surprisingly, our perovskite-type electrodes show a very similar electrochemical as well as spectroscopic behavior, but electronic surface states comparable to the Ce^{3+} are not necessarily evident, and other sources of electrons (e.g., singly charged vacancies) may also be relevant.

For ceria surfaces, also formation of a tridentate carbonate was reported in literature reports based on DFT calculations.[89] For perovskite surfaces, however, no comparable study exists dealing with the conformation of surface carbonates. For an unambiguous proof of the model suggested in this study, further studies are urgently needed to address the question of the mechanism of CO_2 splitting on perovskite-type electrodes in more detail. For example, vibrational spectroscopy may be an additional experimental method for future investigations of the carbonate species, which could shed further light on the reaction mechanism.[11,90] However, on the basis of the already available data we suggest that CO_2 reduction with activation via a $(CO_3)^{\bullet 3-}$ species requires an oxide electrode with many oxygen vacancies but also with sufficiently high electron concentration. High oxygen vacancy concentrations are generally achieved by acceptor doping. Then, however, electron concentration is often strongly suppressed by high hole concentrations. Our model with the requirement of both electrons and oxygen vacancies thus provides the first information regarding how to further proceed in the search for improved perovskite-type CO_2 reduction electrodes.

Regarding the following steps of the CO_2 electrolysis a second electron transfer as well as release of CO is necessary.

$$(CO_3)^{\bullet 3-}(ad) + e^- \rightarrow CO(gas) + 2O^{2-} \quad (10)$$

Under very strong cathodic polarization and thus very high electron concentration in the mixed conducting perovskites, the rate-limiting step of eq 10 is accelerated electrochemically, thus leading to the observed decrease of carbonate coverage, which is observed for LSF and LSCrNi7291 in Figure 8. This assumption of electron concentration directly affecting kinetics of the rate-determining step is supported by the exponential current voltage kinetics (see Figure 2) together with the observed −1 eV/V binding energy shift of the carbonate intermediate (see Figure 7a). The fact that the carbonate completely follows the Fermi level shifts upon polarization clearly rules out the possibility of a Butler−Volmer-type mechanism, where the applied polarization changes the activation barrier of the rate-limiting charge transfer step thus yielding the typical exponential U−I curves.[60] On solid state electrodes such a type of mechanism can only occur if there exists an electrostatic surface potential step such as a surface dipole.[61] If such a surface dipole is affected by the applied electrochemical polarization the binding energy of the respective species shifts by value different from −1 eV/V.[30,35] The observed exponential U−I curve can thus not be explained by the applied polarization modifying an activation energy barrier. Rather, an increase in electron concentration accelerating the rate-determining step is a possible scenario. Since the concentration of electrons in the studied perovskites depends exponentially on the applied cathodic overpotential, a rate-determining elementary step depending on the concentration of electrons in the electrode material is a very likely explanation for the observed behavior.

For completing the reaction cycle the surface of the perovskite has to be recovered by again forming a surface oxygen vacancy. In contrast to purely chemically driven CO_2 conversion, where often hydrogen is employed for this purpose, electrochemically driven CO_2 splitting regenerates the surface by vacancies formed at the counter electrode via

DOI: 10.1021/acsami.7b10673
ACS Appl. Mater. Interfaces 2017, 9, 35847−35860

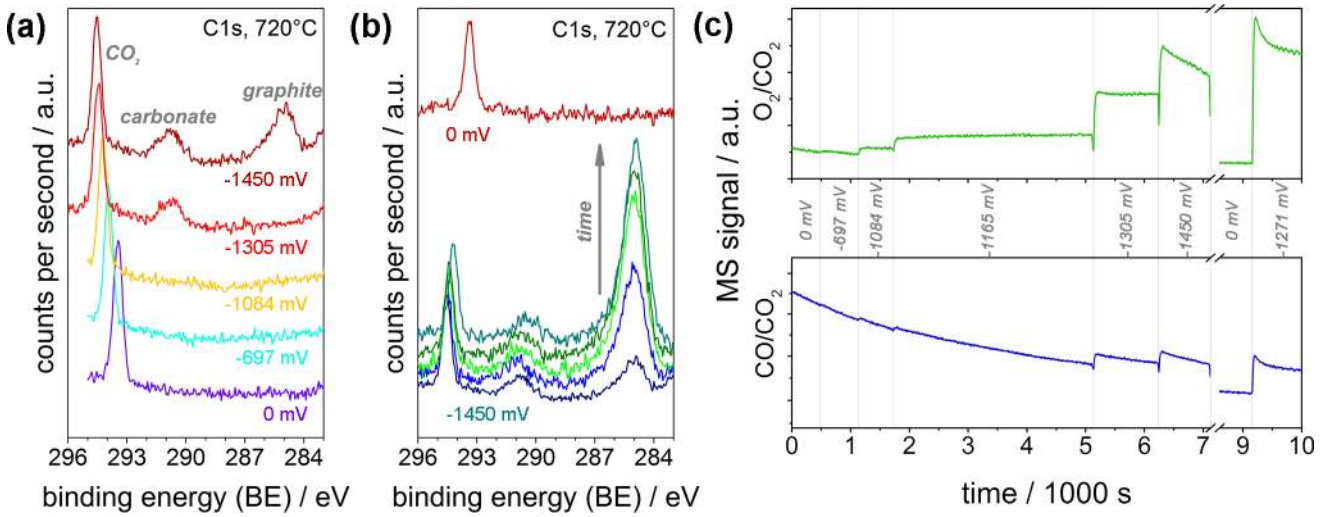

Figure 10. (a) C 1s spectra measured on LSCrNi8291 at 720 °C in 0.25 mbar CO_2 at different cathodic polarizations. Coking occurs at the highest overpotential (η = −1450 mV) observable by evolution of an asymmetric peak at 284−285 eV. (b) With prolonged time the amount of deposited graphite increases, but it is immediately removed upon retracting the polarization. (BE in parts a and b not corrected.) (c) MS signals of O_2 and CO (normalized to CO_2 background) with visible steps corresponding to the indicated overpotential.

$$2O^{2-} \rightarrow O_2(gas) + 4e^- + 2Vac \quad (11)$$

These vacancies are then transported to the working electrode surface due to the electrochemical potential difference applied to the electrolysis cell. At the working electrode they can again start a CO_2 splitting reaction. This method of electrochemically regenerating active surface sites can be much more efficient than a purely chemical reduction, since no additional reduction agent such as H_2 is needed; thus, no competition of different gas species for adsorption sites takes place, and the byproducts (H_2O in case of chemical reduction, O_2 in the present case) can easily be prevented from contaminating the produced CO by separating the gas compartments of working and counter electrodes. These advantages further highlight the attractiveness of electrochemical CO_2 splitting and thus emphasize the need for an in-depth understanding of this reaction, especially on oxide electrodes.

3.6. Coking and Regeneration Effects. The deposition of carbon was only observed under very strong electrochemical polarization. Figure 10a depicts C 1s spectra measured on a LSCrNi8291 working electrode at 720 °C in 0.25 mbar CO_2 under different cathodic overpotentials. Only under 1450 mV does an additional asymmetric peak at 284−285 eV appear, which is characteristic for graphitic carbon.[70] When keeping the polarization, this peak grows further, as shown in Figure 10b. The fact that carbon deposition also occurs at these relatively high temperatures and with a pure CO_2 gas feed can be explained by the extremely reducing conditions established by the strong cathodic polarization. Under these conditions the local CO partial pressure at the electrode surface is very high thus allowing carbon formation by CO disproportionation ($2CO(ad) \rightarrow C(ad) + CO_2$) or by a direct electrochemical reduction of carbon monoxide ($CO(ad) + 2e- \rightarrow C(ad) + O^{2-}$). However, upon retraction of the applied potential, the graphite peak immediately disappears, indicating a complete removal of the carbon deposit from the electrode surface (see also Figure 10b, top spectrum). A very similar behavior was also found on LSF electrodes, as shown in Figure S7 in the Supporting Information. Compared to zirconia or ceria based state of the art SOFC/SOEC fuel electrodes, where relatively harsh oxidizing conditions (which may also oxidize the Ni particles and lead to electrode damage) are needed to fully remove carbon deposits,[91,92] the regeneration on our perovskites is thus easy to achieve.

The quick removal of carbon can be explained by reaction of the carbon deposit with CO_2 from the gas phase via the reversed Boudouard reaction ($C + CO_2 \rightarrow 2CO$). At the experimental temperature of 720 °C the "CO side" of the reaction is thermodynamically favored.[65] Differences in the regeneration behavior may originate from different types of carbon (such as graphitic carbon, disordered carbon, carbon nanotubes, and others) growing on different electrode materials. How far the metallic exsolutions play a role in the regeneration behavior cannot be concluded unambiguously from the data available so far; this question needs to be addressed in future work.

The electrochemical effects caused by carbon deposition can also be observed in current voltage curves (see open symbols in Figure 2a) and in the amount of produced O_2 (and CO) as shown in Figure 10c: Under 1450 mV overpotential the production rate of O_2 significantly decreased with time. MS data also nicely reflect the regeneration effect upon retracting the applied bias: When reapplying a cathodic voltage (1271 mV at ca. 9200 s in Figure 10c) the O_2 production rate was even slightly higher than that before any coking had occurred (which might be due to a slightly increased roughness of the working electrodes). This again demonstrates the complete reversibility of the detrimental effects of carbon deposition, which is advantageous from an application point of view.

4. CONCLUSION

High temperature electrolysis of carbon dioxide was performed on different acceptor doped perovskite-type electrodes. In contrast to recent publications dealing with CO_2 electrolysis on porous perovskite electrodes, the present work employs geometrically well-defined thin film electrodes. These model-type electrodes not only allow reliable comparison of electrode performance but also facilitate NAP-XPS measurements to study the surface chemistry of the electrodes under operation conditions. From the combined interpretation of the electro-

DOI: 10.1021/acsami.7b10673
ACS Appl. Mater. Interfaces 2017, 9, 35847−35860

chemical results and the XPS data, the following conclusions are drawn:

- All investigated electrode materials exhibit exponential current−voltage characteristics with LSF electrodes showing higher performance than chromite based materials. However, the virtually identical slopes in Tafel plots suggest that the reaction mechanism of CO_2 reduction is the same on all investigated materials.
- Exsolution of metallic particles from the perovskite lattice does not affect the kinetics of CO_2 splitting, in contrast to high temperature H_2O electrolysis. This contradicts conclusions made from electrochemical CO_2 splitting measurements with porous perovskite electrodes and illustrates the importance of *operando* spectroscopic characterization of carbon dioxide electrolysis on model-type electrodes.
- CO_2 electrolysis on all investigated materials proceeds via a carbonate intermediate populating on the oxide surface under sufficiently reducing (cathodic) conditions. The carbonate adsorbate is interpreted as a bidentate radical $(CO_3)^{\bullet 3-}$, which forms via adsorption of CO_2 on oxygen vacancies in combination with an electron transfer step. The electron originates from either a polaron or a singly charged oxygen vacancy.
- In particular, the chromite based electrode materials exhibit a rather high coking resilience with carbon deposition only occurring under strongly cathodic polarization. Moreover, the detrimental effects of carbon are completely reversible upon retracting the applied bias without damaging the electrode, which is very promising from an application point of view.

■ ASSOCIATED CONTENT

Supporting Information

The Supporting Information is available free of charge on the ACS Publications website at DOI: 10.1021/acsami.7b10673.

Additional information on impedance spectroscopy, *I*−*V* characteristics, SEM, XPS data interpretation, and coking and regeneration of LSF (PDF)

■ AUTHOR INFORMATION

Corresponding Author

*E-mail: alexander.opitz@tuwien.ac.at.

ORCID

Alexander K. Opitz: 0000-0002-2567-1885
Markus Kubicek: 0000-0001-6623-9805
Thomas Götsch: 0000-0003-3673-317X

Present Address

[⊥]Department of Materials Science and Engineering, Massachusetts Institute of Technology, 77 Massachusetts Avenue, Cambridge, MA 02139, United States.

Funding

This study was financially supported by the Austrian Science Fund (FWF) through Grants F45-02/03/09 (SFB FOXSI) and W1243. Moreover, C.R. and T.G. thankfully acknowledge the financial support by HZB through travel grants.

Notes

The authors declare no competing financial interest.

■ ACKNOWLEDGMENTS

The authors thank the Helmholtz-Zentrum Berlin for the allocation of beamtime at beamline ISISS-PGM of synchrotron BESSY II and the BESSY staff for their assistance during the beamtime. SEM investigations were carried out using facilities at the University Service Centre for Transmission Electron Microscopy, Vienna University of Technology, Austria; Elisabeth Eitenberger is gratefully acknowledged for her help recording the SEM images. A.K.O. thanks Jiayue Wang (MIT) for helpful discussions.

■ REFERENCES

(1) Lewis, N. S.; Nocera, D. G. Powering the Planet: Chemical Challenges in Solar Energy Utilization. *Proc. Natl. Acad. Sci. U. S. A.* **2006**, *103*, 15729−15735.

(2) Krol, R. v. d.; Grätzel, M. In *Photoelectrochemical Hydrogen Production*; Tuller, H. L., Ed.; Springer: New York, 2012; p 321.

(3) Kurzweil, P. HISTORY|Electrochemistry. In *Encyclopedia of Electrochemical Power Sources*; Elsevier: Amsterdam, 2009; pp 533−554.

(4) Pöhlmann, F.; Jess, A. Influence of Syngas Composition on the Kinetics of Fischer−Tropsch Synthesis of using Cobalt as Catalyst. *Energy Technol.* **2016**, *4*, 55−64.

(5) Graves, C.; Ebbesen, S. D.; Mogensen, M.; Lackner, K. S. Sustainable Hydrocarbon Fuels by Recycling CO2 and H2O with Renewable or Nuclear Energy. *Renewable Sustainable Energy Rev.* **2011**, *15*, 1−23.

(6) Rostrup-Nielsen, J.; Christiansen, L. J. *Concepts in Syngas Manufacture*; Imperial College Press: London, 2011; Vol. *10*, p 392.

(7) Tao, G.; Sridhar, K. R.; Chan, C. L. Study of Carbon Dioxide Electrolysis at Electrode/Electrolyte Interface: Part I. Pt/YSZ Interface. *Solid State Ionics* **2004**, *175*, 615−619.

(8) Isenberg, A. O. *Three-Man Solid Electrolyte Carbon Dioxide Electrolysis Breadboard (Report No. CR-185612)*; NASA-CR-185612; NASA Research Center; Jun 01, 1989.

(9) Ebbesen, S. D.; Jensen, S. H.; Hauch, A.; Mogensen, M. B. High Temperature Electrolysis in Alkaline Cells, Solid Proton Conducting Cells, and Solid Oxide Cells. *Chem. Rev.* **2014**, *114*, 10697−10734.

(10) Ebbesen, S. D.; Mogensen, M. Electrolysis of carbon dioxide in Solid Oxide Electrolysis Cells. *J. Power Sources* **2009**, *193*, 349−358.

(11) Freund, H. J.; Roberts, M. W. Surface Chemistry of Carbon Dioxide. *Surf. Sci. Rep.* **1996**, *25*, 225−273.

(12) Durst, J.; Rudnev, A.; Dutta, A.; Fu, Y.; Herranz, J.; Kaliginedi, V.; Kuzume, A.; Permyakova, A. A.; Paratcha, Y.; Broekmann, P.; Schmidt, T. J. Electrochemical CO2 Reduction: A Critical View on Fundamentals, Materials and Applications. *Chimia* **2015**, *69*, 769−776.

(13) Springer, T. E.; Rockward, T.; Zawodzinski, T. A.; Gottesfeld, S. Model for Polymer Electrolyte Fuel Cell Operation on Reformate Feed: Effects of CO, H2 Dilution, and High Fuel Utilization. *J. Electrochem. Soc.* **2001**, *148*, A11−A23.

(14) Tao, G.; Sridhar, K. R.; Chan, C. L. Study of Carbon Dioxide Electrolysis at Electrode/Electrolyte Interface: Part II. Pt-YSZ Cermet/YSZ Interface. *Solid State Ionics* **2004**, *175*, 621−624.

(15) Ruiz-Trejo, E.; Irvine, J. T. S. Electrolysis of CO2 in a Proton Conducting Membrane. *Solid State Ionics* **2013**, *252*, 157−164.

(16) Singh, V.; Muroyama, H.; Matsui, T.; Hashigami, S.; Inagaki, T.; Eguchi, K. Feasibility of Alternative Electrode Materials for High Temperature CO2 Reduction on Solid Oxide Electrolysis Cell. *J. Power Sources* **2015**, *293*, 642−648.

(17) Mahmood, A.; Bano, S.; Yu, J. H.; Lee, K.-H. High-Performance Solid Oxide Electrolysis Cell Based on ScSZ/GDC (Scandia-Stabilized Zirconia/Gadolinium-Doped Ceria) Bi-Layered Electrolyte and LSCF (Lanthanum Strontium Cobalt Ferrite) Oxygen Electrode. *Energy* **2015**, *90*, 344−350.

(18) Hauch, A.; Brodersen, K.; Chen, M.; Mogensen, M. B. Ni/YSZ Electrode Structures Optimized for Increased Electrolysis Performance and Durability. *Solid State Ionics* **2016**, *293*, 27−36.

DOI: 10.1021/acsami.7b10673
ACS Appl. Mater. Interfaces 2017, 9, 35847−35860

(19) Xie, Y.; Xiao, J.; Liu, D.; Liu, J.; Yang, C. Electrolysis of Carbon Dioxide in a Solid Oxide Electrolyzer with Silver-Gadolinium-Doped Ceria Cathode. *J. Electrochem. Soc.* **2015**, *162*, F397−F402.
(20) Cheng, C.-Y.; Kelsall, G. H.; Kleiminger, L. Reduction of CO2 to CO at Cu−Ceria-Gadolinia (CGO) Cathode in Solid Oxide Electrolyser. *J. Appl. Electrochem.* **2013**, *43*, 1131−1144.
(21) Green, R. D.; Liu, C.-C.; Adler, S. B. Carbon Dioxide Reduction on Gadolinia-Doped Ceria Cathodes. *Solid State Ionics* **2008**, *179*, 647−660.
(22) Yue, X.; Irvine, J. T. S. Alternative Cathode Material for CO2 Reduction by High Temperature Solid Oxide Electrolysis Cells. *J. Electrochem. Soc.* **2012**, *159*, F442−F448.
(23) Bidrawn, F.; Kim, G.; Corre, G.; Irvine, J. T. S.; Vohs, J. M.; Gorte, R. J. Efficient Reduction of CO2 in a Solid Oxide Electrolyzer. *Electrochem. Solid-State Lett.* **2008**, *11*, B167−B170.
(24) Zhang, X.; Ye, L.; Hu, J.; Li, J.; Jiang, W.; Tseng, C.-J.; Xie, K. Perovskite LSCM Impregnated with Vanadium Pentoxide for High Temperature Carbon Dioxide Electrolysis. *Electrochim. Acta* **2016**, *212*, 32−40.
(25) Xie, K.; Zhang, Y.; Meng, G.; Irvine, J. T. S. Direct Synthesis of Methane from CO2/H2O in an Oxygen-Ion Conducting Solid Oxide Electrolyser. *Energy Environ. Sci.* **2011**, *4*, 2218−2222.
(26) Yu, Y.; Mao, B.; Geller, A.; Chang, R.; Gaskell, K.; Liu, Z.; Eichhorn, B. W. CO2 Activation and Carbonate Intermediates: An Operando AP-XPS Study of CO2 Electrolysis Reactions on Solid Oxide Electrochemical Cells. *Phys. Chem. Chem. Phys.* **2014**, *16*, 11633−11639.
(27) Feng, Z. A.; Machala, M. L.; Chueh, W. C. Surface Electrochemistry of CO2 Reduction and CO Oxidation on Sm-doped CeO2-x: Coupling Between Ce3+ and Carbonate Adsorbates. *Phys. Chem. Chem. Phys.* **2015**, *17*, 12273−12281.
(28) Yurkiv, V.; Starukhin, D.; Volpp, H.-R.; Bessler, W. G. Elementary Reaction Kinetics of the CO/CO2/Ni/YSZ Electrode. *J. Electrochem. Soc.* **2011**, *158*, B5−B10.
(29) Crumlin, E. J.; Liu, Z.; Bluhm, H.; Yang, W.; Guo, J.; Hussain, Z. X-ray Spectroscopy of Energy Materials Under In Situ/Operando Conditions. *J. Electron Spectrosc. Relat. Phenom.* **2015**, *200*, 264−273.
(30) Zhang, C.; Yu, Y.; Grass, M. E.; Dejoie, C.; Ding, W.; Gaskell, K.; Jabeen, N.; Hong, Y. P.; Shavorskiy, A.; Bluhm, H.; Li, W.-X.; Jackson, G. S.; Hussain, Z.; Liu, Z.; Eichhorn, B. W. Mechanistic Studies of Water Electrolysis and Hydrogen Electro-Oxidation on High Temperature Ceria-Based Solid Oxide Electrochemical Cells. *J. Am. Chem. Soc.* **2013**, *135*, 11572−11579.
(31) Mueller, D. N.; Machala, M. L.; Bluhm, H.; Chueh, W. C. Redox Activity of Surface Oxygen Anions in Oxygen-Deficient Perovskite Oxides During Electrochemical Reactions. *Nat. Commun.* **2015**, *6*, 6097.
(32) Crumlin, E. J.; Mutoro, E.; Hong, W. T.; Biegalski, M. D.; Christen, H. M.; Liu, Z.; Bluhm, H.; Shao-Horn, Y. In Situ Ambient Pressure X-ray Photoelectron Spectroscopy of Cobalt Perovskite Surfaces under Cathodic Polarization at High Temperatures. *J. Phys. Chem. C* **2013**, *117*, 16087−16094.
(33) Liu, S.; Liu, Q.; Luo, J.-L. Highly Stable and Efficient Catalyst with In Situ Exsolved Fe−Ni Alloy Nanospheres Socketed on an Oxygen Deficient Perovskite for Direct CO2 Electrolysis. *ACS Catal.* **2016**, *6*, 6219−6228.
(34) Crumlin, E. J.; Bluhm, H.; Liu, Z. In situ Investigation of Electrochemical Devices Using Ambient Pressure Photoelectron Spectroscopy. *J. Electron Spectrosc. Relat. Phenom.* **2013**, *190* (A), 84−92.
(35) Feng, Z. A.; Balaji Gopal, C.; Ye, X.; Guan, Z.; Jeong, B.; Crumlin, E.; Chueh, W. C. Origin of Overpotential-Dependent Surface Dipole at CeO2−x/Gas Interface During Electrochemical Oxygen Insertion Reactions. *Chem. Mater.* **2016**, *28*, 6233−6242.
(36) Opitz, A. K.; Nenning, A.; Rameshan, C.; Rameshan, R.; Blume, R.; Hävecker, M.; Knop-Gericke, A.; Rupprechter, G.; Fleig, J.; Klötzer, B. Enhancing Electrochemical Water-Splitting Kinetics by Polarization-Driven Formation of Near-Surface Iron(0): An In Situ XPS Study on Perovskite-Type Electrodes. *Angew. Chem., Int. Ed.* **2015**, *54*, 2628−2632.
(37) Goodenough, J. B.; Huang, Y.-H. Alternative Anode Materials for Solid Oxide Fuel Cells. *J. Power Sources* **2007**, *173*, 1−10.
(38) Neagu, D.; Tsekouras, G.; Miller, D. N.; Ménard, H.; Irvine, J. T. S. In Situ Growth of Nanoparticles Through Control of Non-Stoichiometry. *Nat. Chem.* **2013**, *5*, 916−923.
(39) Cowin, P. I.; Petit, C. T. G.; Lan, R.; Irvine, J. T. S.; Tao, S. Recent Progress in the Development of Anode Materials for Solid Oxide Fuel Cells. *Adv. Energy Mater.* **2011**, *1*, 314−332.
(40) Tsipis, E. V.; Kharton, V. V. Electrode Materials and Reaction Mechanisms in Solid Oxide Fuel Cells: A Brief Review. *J. Solid State Electrochem.* **2008**, *12*, 1367−1391.
(41) Bierschenk, D. M.; Barnett, S. A. Electrochemical Characteristics of La0.8Sr0.2Cr0.82Ru0.18O3−δ−Gd0.1Ce0.9O2 Solid Oxide Fuel Cell Anodes in H2−H2O−CO−CO2 Fuel Mixtures. *J. Power Sources* **2012**, *201*, 95−102.
(42) Katz, M. B.; Graham, G. W.; Duan, Y.; Liu, H.; Adamo, C.; Schlom, D. G.; Pan, X. Self-Regeneration of Pd−LaFeO3 Catalysts: New Insight from Atomic-Resolution Electron Microscopy. *J. Am. Chem. Soc.* **2011**, *133*, 18090−18093.
(43) Li, Y.; Wang, Y.; Doherty, W.; Xie, K.; Wu, Y. Perovskite Chromates Cathode with Exsolved Iron Nanoparticles for Direct High-Temperature Steam Electrolysis. *ACS Appl. Mater. Interfaces* **2013**, *5*, 8553−8562.
(44) Nishihata, Y.; Mizuki, J.; Akao, T.; Tanaka, H.; Uenishi, M.; Kimura, M.; Okamoto, T.; Hamada, N. Self-Regeneration of a Pd-Perovskite Catalyst for Automotive Emissions Control. *Nature* **2002**, *418*, 164−167.
(45) Haag, J. M.; Barnett, S. A.; Richardson, J. W.; Poeppelmeier, K. R. Structural and Chemical Evolution of the SOFC Anode La0.30Sr0.70Fe0.70Cr0.30O3−δ upon Reduction and Oxidation: An in Situ Neutron Diffraction Study. *Chem. Mater.* **2010**, *22*, 3283−3289.
(46) Adijanto, L.; Padmanabhan, V. B.; Gorte, R. J.; Vohs, J. M. Polarization-Induced Hysteresis in CuCo-Doped Rare Earth Vanadates SOFC Anodes. *J. Electrochem. Soc.* **2012**, *159*, F751−F756.
(47) Tsekouras, G.; Neagu, D.; Irvine, J. T. S. Step-Change in High Temperature Steam Electrolysis Performance of Perovskite Oxide Cathodes with Exsolution of B-Site Dopants. *Energy Environ. Sci.* **2013**, *6*, 256−266.
(48) Nenning, A.; Opitz, A. K.; Rameshan, C.; Rameshan, R.; Blume, R.; Hävecker, M.; Knop-Gericke, A.; Rupprechter, G.; Klötzer, B.; Fleig, J. Ambient Pressure XPS Study of Mixed Conducting Perovskite-Type SOFC Cathode and Anode Materials under Well-Defined Electrochemical Polarization. *J. Phys. Chem. C* **2016**, *120*, 1461−1471.
(49) Tao, S.; Irvine, J. T. S. Catalytic Properties of the Perovskite Oxide La0.75Sr0.25Cr0.5Fe0.5O3-δ in Relation to its Potential as a Solid Oxide Fuel Cell Anode Material. *Chem. Mater.* **2004**, *16*, 4116−4121.
(50) Tao, S.; Irvine, J. T. S. Synthesis and Characterization of (La0.75Sr0.25)Cr0.5Mn0.5O3-δ, a Redox-Stable, Efficient Perovskite Anode for SOFCs. *J. Electrochem. Soc.* **2004**, *151*, A252−A259.
(51) Raj, E. S.; Irvine, J. T. S. Synthesis and Characterization of (Pr0.75Sr0.25)1-xCr0.5Mn0.5O3-δ as Anode for SOFCs. *Solid State Ionics* **2010**, *180*, 1683−1689.
(52) Yue, X.; Irvine, J. T. S. Impedance Studies on LSCM/GDC Cathode for High Temperature CO2 Electrolysis. *Electrochem. Solid-State Lett.* **2012**, *15*, B31−B34.
(53) Kuhn, M.; Hashimoto, S.; Sato, K.; Yashiro, K.; Mizusaki, J. Oxygen Nonstoichiometry, Thermo-Chemical Stability and Lattice Expansion of La0.6Sr0.4FeO3-δ. *Solid State Ionics* **2011**, *195*, 7−15.
(54) Pechini, M. P. Method of Preparing Lead and Alkaline Earth Titanates and Niobates and Coating Method Using the Same to Form a Capacitor. U.S. Patent 3.330.697, July 11th, 1967.
(55) Kogler, S.; Nenning, A.; Rupp, G. M.; Opitz, A. K.; Fleig, J. Comparison of Electrochemical Properties of La0.6Sr0.4FeO3-δ Thin Film Electrodes: Oxidizing vs. Reducing Conditions. *J. Electrochem. Soc.* **2015**, *162*, F317−F326.

DOI: 10.1021/acsami.7b10673
ACS Appl. Mater. Interfaces 2017, 9, 35847−35860

(56) Nenning, A.; Opitz, A. K.; Huber, T.; Fleig, J. A Novel Approach for Analyzing Electrochemical Properties of Mixed Conducting Solid Oxide Fuel Cell Anode Materials by Impedance Spectroscopy. *Phys. Chem. Chem. Phys.* **2014**, *16*, 22321−22336.
(57) Haevecker, M. Innovative Station for In Situ Spectroscopy. https://www.helmholtz-berlin.de/pubbin/igama_output?modus=einzel&sprache=en&gid=1607&typoid=50740 (accessed 2016-09-26).
(58) Opitz, A. K.; Lutz, A.; Kubicek, M.; Kubel, F.; Hutter, H.; Fleig, J. Investigation of the Oxygen Exchange Mechanism on Pt/YSZ at Intermediate Temperatures: Surface Path versus Bulk Path. *Electrochim. Acta* **2011**, *56*, 9727−9740.
(59) Opitz, A. K.; Fleig, J. Investigation of O2 Reduction on Pt/YSZ by Means of Thin Film Microelectrodes: The Geometry Dependence of the Electrode Impedance. *Solid State Ionics* **2010**, *181*, 684−693.
(60) Hamann, C. H.; Hamnett, A.; Vielstich, W. *Electrochemistry*, 2nd ed.; Wiley-VCH: Weinheim, 2007; p 550.
(61) Fleig, J. On the Current-Voltage Characteristics of Charge Transfer Reactions at Mixed Conducting Electrodes on Solid Electrolytes. *Phys. Chem. Chem. Phys.* **2005**, *7*, 2027−2037.
(62) Fleig, J.; Rupp, G. M.; Nenning, A.; Schmid, A. Towards an Improved Understanding of Electrochemical Oxygen Exchange Reactions on Mixed Conducting Oxides. *ECS Trans.* **2017**, *77*, 93−108.
(63) Carbon Dioxide. http://webbook.nist.gov/cgi/inchi/InChI%3D1S/CO2/c2-1-3 (accessed 2017-03-20).
(64) Janek, J.; Korte, C. Electrochemical Blackening of Yttria-Stabilized Zirconia - Morphological Instability of the Moving Reaction Front. *Solid State Ionics* **1999**, *116*, 181−195.
(65) Lide, D. R. *CRC Handbook of Chemistry and Physics*, 85th ed.; CRC Press: Boca Raton, 2004−2005; p 2712.
(66) Deng, X.; Verdaguer, A.; Herranz, T.; Weis, C.; Bluhm, H.; Salmeron, M. Surface Chemistry of Cu in the Presence of CO2 and H2O. *Langmuir* **2008**, *24*, 9474−9478.
(67) Staudt, T.; Lykhach, Y.; Tsud, N.; Skála, T.; Prince, K. C.; Matolín, V.; Libuda, J. Electronic Structure of Magnesia−Ceria Model Catalysts, CO2 Adsorption, and CO2 Activation: A Synchrotron Radiation Photoelectron Spectroscopy Study. *J. Phys. Chem. C* **2011**, *115*, 8716−8724.
(68) Bluhm, H. Photoelectron Spectroscopy of Surfaces Under Humid Conditions. *J. Electron Spectrosc. Relat. Phenom.* **2010**, *177*, 71−84.
(69) Porsgaard, S.; Jiang, P.; Borondics, F.; Wendt, S.; Liu, Z.; Bluhm, H.; Besenbacher, F.; Salmeron, M. Charge State of Gold Nanoparticles Supported on Titania under Oxygen Pressure. *Angew. Chem., Int. Ed.* **2011**, *50*, 2266−2269.
(70) Blume, R.; Rosenthal, D.; Tessonnier, J.-P.; Li, H.; Knop-Gericke, A.; Schlögl, R. Characterizing Graphitic Carbon with X-ray Photoelectron Spectroscopy: A Step-by-Step Approach. *ChemCatChem* **2015**, *7*, 2871−2881.
(71) Mutoro, E.; Crumlin, E. J.; Biegalski, M. D.; Christen, H. M.; Shao-Horn, Y. Enhanced Oxygen Reduction Activity on Surface-Decorated Perovskite Thin Films for Solid Oxide Fuel Cells. *Energy Environ. Sci.* **2011**, *4*, 3689−3696.
(72) van der Heide, P. A. W. Systematic X-Ray Photoelectron Spectroscopic Study of La1−xSrx-based Perovskite-Type Oxides. *Surf. Interface Anal.* **2002**, *33*, 414−425.
(73) Cai, Z.; Kubicek, M.; Fleig, J.; Yildiz, B. Chemical Heterogeneities on La0.6Sr0.4CoO3−δ Thin Films—Correlations to Cathode Surface Activity and Stability. *Chem. Mater.* **2012**, *24*, 1116−1127.
(74) Rameshan, C.; Ng, M. L.; Shavorskiy, A.; Newberg, J. T.; Bluhm, H. Water Adsorption on Polycrystalline Vanadium from Ultra-High Vacuum to Ambient Relative Humidity. *Surf. Sci.* **2015**, *641*, 141−147.
(75) Naumkin, A. V.; Kraut-Vass, A.; Gaarenstroom, S. W.; Powell, C. J. *NIST X-ray Photoelectron Spectroscopy Database, Version 4.1*; National Institute of Standards and Technology: Gaithersburg, MD, 2012.
(76) Moulder, J. F.; Stickle, W. F.; Sobol, P. E.; Bomben, K. D. *Handbook of X-ray Photoelectron Spectroscopy: A Reference Book of Standard Spectra for Identification and Interpretation of XPS Data*; Physical Electronics Division, Perkin-Elmer Corporation: Eden Prairie, MN, 1992; p 261.
(77) Ye, L.; Zhang, M.; Huang, P.; Guo, G.; Hong, M.; Li, C.; Irvine, J. T. S.; Xie, K. Enhancing CO2 Electrolysis Through Synergistic Control of Non-Stoichiometry and Doping to Tune Cathode Surface Structures. *Nat. Commun.* **2017**, *8*, 14785.
(78) Kobsiriphat, W.; Madsen, B. D.; Wang, Y.; Shah, M.; Marks, L. D.; Barnett, S. A. Nickel- and Ruthenium-Doped Lanthanum Chromite Anodes: Effects of Nanoscale Metal Precipitation on Solid Oxide Fuel Cell Performance. *J. Electrochem. Soc.* **2010**, *157*, B279−B284.
(79) WebCrossSections. https://vuo.elettra.eu/services/elements/WebElements.html (accessed November 11th 2016).
(80) Young, V.; Otagawa, T. XPS Studies on Strontium Compounds. *Appl. Surf. Sci.* **1985**, *20*, 228−248.
(81) Christie, A. B.; Sutherland, I.; Walls, J. M. An XPS Study of Ion-induced Dissociation on Metal Carbonate Surfaces. *Vacuum* **1981**, *31*, 513−517.
(82) Ritzmann, A. M.; Muñoz-García, A. B.; Pavone, M.; Keith, J. A.; Carter, E. A. Ab Initio DFT+U Analysis of Oxygen Vacancy Formation and Migration in La1-xSrxFeO3-δ (x = 0, 0.25, 0.50). *Chem. Mater.* **2013**, *25*, 3011−3019.
(83) Yoon, S.; Dornseiffer, J.; Xiong, Y.; Grüner, D.; Shen, Z.; Iwaya, S.; Pithan, C.; Waser, R. Synthesis, Spark Plasma Sintering and Electrical Conduction Mechanism in BaTiO3−Cu Composites. *J. Eur. Ceram. Soc.* **2011**, *31*, 773−782.
(84) Berglund, C. N.; Braun, H. J. Optical Absorption in Single-Domain Ferroelectric Barium Titanate. *Phys. Rev.* **1967**, *164*, 790−799.
(85) Setvin, M.; Franchini, C.; Hao, X.; Schmid, M.; Janotti, A.; Kaltak, M.; Van de Walle, C. G.; Kresse, G.; Diebold, U. Direct View at Excess Electrons in TiO2 Rutile and Anatase. *Phys. Rev. Lett.* **2014**, *113*, 086402.
(86) Zolotoyabko, E.; Caspi, E. N.; Fieramosca, J. S.; Von Dreele, R. B. Bond Lengths Differences Between the Mollusk-Made and Geological Calcium Carbonate. *Mater. Sci. Eng., A* **2009**, *524*, 77−81.
(87) Madix, R. J.; Solomon, J. L.; Stöhr, J. The Orientation of the Carbonate Anion on Ag(110). *Surf. Sci.* **1988**, *197*, L253−L259.
(88) Gopal, C. B.; Gabaly, F. E.; McDaniel, A. H.; Chueh, W. C. Origin and Tunability of Unusually Large Surface Capacitance in Doped Cerium Oxide Studied by Ambient-Pressure X-Ray Photoelectron Spectroscopy. *Adv. Mater.* **2016**, *28*, 4692−4697.
(89) Albrecht, P. M.; Jiang, D.-e.; Mullins, D. R. CO2 Adsorption as a Flat-Lying, Tridentate Carbonate on CeO2(100). *J. Phys. Chem. C* **2014**, *118*, 9042−9050.
(90) Foettinger, K.; Schloegl, R.; Rupprechter, G. The Mechanism of Carbonate Formation on Pd-Al2O3 Catalysts. *Chem. Commun.* **2008**, 320−322.
(91) Li, X.; Liu, M.; Lee, J.-p.; Ding, D.; Bottomley, L. A.; Park, S.; Liu, M. An Operando Surface Enhanced Raman Spectroscopy (SERS) Study of Carbon Deposition on SOFC Anodes. *Phys. Chem. Chem. Phys.* **2015**, *17*, 21112−21119.
(92) Subotić, V.; Schluckner, C.; Schroettner, H.; Hochenauer, C. Analysis of Possibilities for Carbon Removal from Porous Anode of Solid Oxide Fuel Cells After Different Failure Modes. *J. Power Sources* **2016**, *302*, 378−386.

DOI: 10.1021/acsami.7b10673
ACS Appl. Mater. Interfaces 2017, 9, 35847−35860